Electric Field Calculation During Voltage Transients in HVDC Cables: Contribution of Polarization Processes

P. Cambareri, C. de Falco, L. Di Rienzo, *Senior Member, IEEE*, P. Seri, and G. C. Montanari, *Fellow, IEEE*

***Abstract*—The simulation of electric field transients in HVDC cables can be a fundamental tool to support insulation system design when operation dynamics, which includes voltage polarity inversions and load variation, becomes significant during the expected cable life. The field behavior during voltage and temperature transients is associated with intrinsic and extrinsic ageing processes that can affect the cable design life. Traditional models employed for electric field simulations consider only the non–linear, steady–state dependence of conductivity on temperature and field magnitude, but they neglect the transient behavior of permittivity and conductivity, that is, polarization and charge trapping phenomena. These processes impact on the duration of the field transient and thus ageing. This paper discusses the numerical implementation of an electro–quasistatic model that can be used to perform transient simulations of electric fields in HVDC cables insulation. With respect to the model traditionally employed, the presented one is extended with Debye's equations for dielectric polarization processes. The model is implemented numerically using finite differences, or the Occhini equivalent circuit: this paper demonstrates that the two approaches are equivalent. Numerical simulations show that, during transients, polarization processes slow down the electric field dynamics and reduce its maximum intensity.**

***Index Terms*—HVDC insulation, cable insulation, electric fields, dielectric polarization, cable insulation aging.**

I. INTRODUCTION

HIGH VOLTAGE Direct Current (HVDC) cables constitute an important technological asset to operate a highly efficient transmission of electric power over long distances. A major concern in the design of such cables is the ability to guarantee their operational activity for a sufficiently long time, e.g., 30 years, at very low failure probability, e.g., 0.5%. The main difficulty that hinders the achievement of this goal is the design of the insulation system, notoriously the weakest component of an electric system. Organic insulation systems can age under DC electrothermal stress, due to both intrinsic phenomena (driven by DC field magnitude) and extrinsic accelerated aging mechanisms, as those associated with space charge (SC) accumulation and partial discharges (PD) [1]. Both SC and PD have a strict connection with the distribution of the electric field inside the insulation: SC can cause local magnification of the field [2], while PD are trigged when the field level exceeds a certain threshold [3]. To estimate the cable lifetime and optimize the design of the insulation system, it is important to perform accurate simulations of electric fields, especially during transients. Modern HVDC lines experience frequent voltage and load transients, therefore the accelerated aging mechanisms that can be triggered by such repetitive transients cannot be neglected in insulation design and reliability estimation [4, 5, 6]. The traditional model used to simulate electric fields in DC insulation is given by [2] and reads

$$\begin{cases} \rho + \nabla \cdot (\varepsilon_\infty \nabla \varphi) = 0 \\ \frac{\partial \rho}{\partial t} - \nabla \cdot (\sigma(E,T) \nabla \varphi) = 0 \end{cases}, \tag{1}$$

where ρ is the charge density, φ is the electric scalar potential related to the electric field via $\boldsymbol{E} = -\nabla\varphi$, ε_∞ and σ are the medium permittivity and conductivity. The first equation in (1) is Gauss' law $\nabla \cdot \boldsymbol{D} = \rho$, with $\boldsymbol{D} = \varepsilon_\infty \boldsymbol{E}$; the second one is the continuity equation $\partial_t \rho + \nabla \cdot \boldsymbol{J} = 0$, with $\boldsymbol{J} = \sigma \boldsymbol{E}$. The permittivity ε_∞ is assumed constant, while for the conductivity a semi–empirical model is adopted, [2, 7, 8], i.e.

$$\sigma(T,E) = \sigma_0 \exp\left(-\frac{\alpha}{T} + \beta |E|\right), \tag{2}$$

where T is the temperature and $\boldsymbol{E}$ is the electric field intensity. If polarization processes are considered in (1), we obtain [9]

$$\begin{cases} \rho + \nabla \cdot (\varepsilon_\infty \nabla \varphi - \sum_{k=1}^{N} \boldsymbol{P}_k) = 0 \\ \frac{\partial \rho}{\partial t} - \nabla \cdot (\sigma(T,E) \nabla \varphi) = 0 \\ \tau_k \frac{\partial \boldsymbol{P}_k}{\partial t} + \boldsymbol{P}_k = -\varepsilon_0 \chi_k \nabla \varphi \quad k = 1, \dots, N \end{cases} \tag{3}$$

where the electric displacement field $\boldsymbol{D} = \varepsilon_\infty \boldsymbol{E} + \sum_{k=1}^{N} \boldsymbol{P}_k$ includes the contribution of "fast" polarization processes, $\varepsilon_\infty \boldsymbol{E}$, whose adaptation to the electric field is assumed instantaneous, and of "slow" processes, $\boldsymbol{P}_k$, which adapt to $\boldsymbol{E}$ according to the Debye relaxation model [10]; χ_k is the process susceptibility and τ_k is its time constant (ε_0 = 8.854·10^{-12} As/(Vm) is the

Corresponding author: P. Cambareri.
P. Cambareri and L. Di Rienzo are with the Dipartimento di Elettronica, Informazione e Bioingegneria, Politecnico di Milano, Milano, Italy (e-mails: pasquale.cambareri@polimi.it and luca.dirienzo@polimi.it). C. de Falco is with the MOX, Dipartimento di Matematica, Politecnico di Milano, Milano, Italy (e-mail: carlo.defalco@polimi.it). P. Seri is with the LIMES, Dipartimento di Ingegneria dell'Energia Elettrica e dell'Informazione, Università di Bologna, Bologna, Italy (e-mail: paolo.seri2@polimi.it). G. C. Montanari is with the Center for Advanced Power Systems, Florida State University, Tallahassee, FL, USA (e-mail: gmontanari@fsu.edu).

vacuum permittivity). According to the theory of dielectric materials [10], the Debye processes imply that the frequency-dependent permittivity can be written as

$$\varepsilon(\omega) = \varepsilon_\infty + \sum_{k=1}^{N} \frac{\varepsilon_0 \chi_k}{1+\omega\tau_k}, \quad (4)$$

where $\varepsilon_\infty = \varepsilon_0 \varepsilon_r = \varepsilon_0(1+\chi_\infty)$ and χ_∞ is the high-frequency susceptibility, while the χ_k are the susceptibilities of the slow polarization processes. The inverse transform of (4) provides the time-dependent permittivity.

Model (1) is widely studied in literature, and it is mainly adopted to evaluate the accumulation of space charge due to the non–uniformity of $\boldsymbol{E}$ and T, which are related, respectively, to geometry and heat transfer. Equation (2), or other alternative empirical formulae, introduce a non–linearity that prevents from obtaining an analytical solution even in 1D geometries. Reference [2] studies (1) coupled with temperature, considering the heating associated to the insulation losses, and proposes an iterative method to handle the non–linearity in (2). References [11] and [12] study (1) coupled with temperature, including insulation losses. Reference [11] focuses on the relation between the non–uniformity of the temperature and the space charge accumulation. In [12] the thermal stability problem is studied in a 1D geometry. A more accurate evaluation of the transient duration is obtained using circuital models [8, 13], typically referred to as the extended Debye model or the Occhini equivalent circuit. Due to their structure, these models are not suitable for multidimensional problems or for the evaluation of electric fields in non–uniform geometries. On the other hand, the parameters of the equivalent circuit in [8] can be easily obtained from Polarization and Depolarization Current (PDC) measurements, as in [13], or, by a better physical basis, as in [9]. In [9, 14, 15] model (3) is used for the study of the electric field transient.

In this paper we discretize (3) in space with a 1D finite–difference method, and we show the relation between the material parameters present in (3) and those of the equivalent circuit of [8, 9]. Using again the analogy between circuital and differential models, for the numerical solution of the electric field transient we use a classic Backward Differentiation Formula (BDF) method to deal with circuital models, which allows to handle accurately and efficiently the non–linearity in (2). To validate the model, we focus on the experimental data of impregnated paper only, due to the dominant polarization processes. The case of polymeric materials will not be considered, because they may exhibit both polarization and charge trapping-detrapping mechanisms, and to account for the latter a more sophisticated model is necessary [16, 17].

The novelty in this paper is that it shows, for the first time, the equivalence between the 1D discretization of (3) and the circuital model, which was typically given for granted in the previous works [8, 9]. This equivalence allows the physical parameters obtained from the PDC experiments performed on dielectric specimens, that are typically investigated using circuital models, to be used to perform calculations with the differential model (3). The advantage of the differential model is that it can be generalized to 2D and 3D geometries, enabling the study of the electric field transient in cables, joints, and other components with more complex geometry. This paper also demonstrates that, during transients, the maximum electric field in HVDC cables is lower when polarization processes are considered, that implies a beneficial effect of such processes on the insulation degradation.

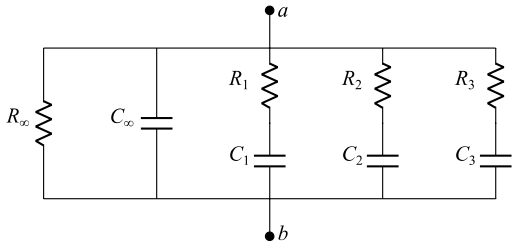

Fig. 1. The Occhini equivalent circuit. This model can be used to describe samples of a material in which polarization processes are predominant.

II. Robustness of the Occhini circuit

The Occhini circuital model, depicted in Fig. 1, can be used to describe the behavior of materials in which polarization processes are predominant. Branches R_k–C_k model the slow polarization processes. With reference to (3) and (4),

$$C_k = \varepsilon_0 \chi_k \frac{A}{d} \quad \text{and} \quad R_k = \frac{\tau_k}{C_k}, \quad (5)$$

where A and d are the area and the thickness of the sample under investigation. C_∞ accounts for the contribution of fast polarization processes, hence,

$$C_\infty = \varepsilon_\infty \frac{A}{d}. \quad (6)$$

R_∞ is associated to the conductivity (2), and it is written as

$$R_\infty = \frac{1}{\sigma} \frac{d}{A}. \quad (7)$$

TABLE I
Measurements from [18, 19, 20]

Sample	Type	T [°C]	E [kV/mm]	A [cm^2]	d [mm]
S1	Single layer	30	0.33	141	1.5
S2	Single layer	60	0.33	141	1.5
S3	Multilayer	20	30	72	0.8
S4	Multilayer	50	12.2	78.5	2.5

Table 1 shows the characteristics of four different samples of impregnated paper for which the experimental PDC were obtained. Measurements were performed on flat specimens, but with different areas, thicknesses, and applied electric fields. Samples S1 and S2 are taken from [18]; they were constituted by a single layer of impregnated paper, which was subjected to a small electric field (0.33 kV/mm). Sample S1 was tested at low temperature (30°C), while S2 at high temperature (60°C). Samples S3 and S4 were made by several layers of impregnated paper stacked upon each other. S3 is taken from [19] and it was tested at high electric field (30 kV/mm) and low temperature (20°C). S4 comes from [20] and was tested at high electric field (12.2 kV/mm) and high temperature (50°C). The peculiarity of

this set of samples is that it covers all the possible working conditions that are encountered in practice for impregnated paper, namely high and low temperatures, high and low electric fields. Single-layer samples S1 and S2 are characterized by typical polarization processes of impregnated paper, i.e., dipolar polarization. Multi-layer samples S3 and S4 may exhibit, in addition, Maxwell-Wagner-Sillars polarization [10], which occurs at the interfaces between the stacked layers. If the Occhini circuit is robust, then it must be able to reproduce all these experiments while satisfying the following constraints:

1) it should use a minimum number of branches R_k–C_k to fit the experiments (e.g. 3), that consider polarization mechanisms involving the orientation of moieties (dipoles) of different nature, and interface phenomena,
2) if the R_k and C_k are fitted from the depolarization characteristic, the same parameters must provide a polarization curve that agrees with the experiments.

The first constraint underlines an important aspect, because with 3 branches we can identify the most relevant polarization processes and divide them into faster, intermediate, and longer processes, according to their time constants $\tau_k = R_k C_k$. This is supported by Table 2, which shows the time constants used to reconstruct the experimental currents shown in Fig. 2 and Fig. 3. Here, 3 branches are sufficient to reproduce the curves in the range 10 – 10^4 s, which is that relevant to these measurements. Fig. 2 compares the measured depolarization curves ("msr") of the samples, with the fitted ones ("fit"). The simulated curves are obtained by a fitting procedure to derive the parameters of the polarization branches, τ_k, C_k and R_k, that works as follows:

1) an initial guess is built with the method shown in [9],
2) a least square optimization is performed to improve the fitting quality.

Tables 3 and 4 show the fitted values for C_k and R_k.

TABLE II
TIME CONSTANTS FITTED FROM MEASUREMENTS IN [18, 19, 20]

τ_k [s]	S1	S2	S3	S4
τ_1	$2.18 \cdot 10^{1}$	$2.70 \cdot 10^{1}$	$3.62 \cdot 10^{1}$	$4.01 \cdot 10^{1}$
τ_2	$2.19 \cdot 10^{2}$	$2.87 \cdot 10^{2}$	$3.00 \cdot 10^{2}$	$4.19 \cdot 10^{2}$
τ_3	$2.57 \cdot 10^{3}$	$1.24 \cdot 10^{3}$	$3.10 \cdot 10^{3}$	$2.84 \cdot 10^{3}$

TABLE III
CAPACITANCES FITTED FROM MEASUREMENTS IN [18, 19, 20]

C_k [F]	S1	S2	S3	S4
C_1	$2.56 \cdot 10^{-11}$	$1.95 \cdot 10^{-10}$	$1.70 \cdot 10^{-11}$	$1.41 \cdot 10^{-11}$
C_2	$6.41 \cdot 10^{-11}$	$4.94 \cdot 10^{-10}$	$3.10 \cdot 10^{-11}$	$4.83 \cdot 10^{-11}$
C_3	$1.84 \cdot 10^{-10}$	$3.90 \cdot 10^{-11}$	$1.28 \cdot 10^{-10}$	$6.76 \cdot 10^{-11}$

TABLE IV
RESISTANCES FITTED FROM MEASUREMENTS IN [18, 19, 20]

R_k [Ω]	S1	S2	S3	S4
R_1	$8.47 \cdot 10^{11}$	$1.38 \cdot 10^{11}$	$2.12 \cdot 10^{12}$	$2.84 \cdot 10^{12}$
R_2	$3.42 \cdot 10^{12}$	$5.84 \cdot 10^{11}$	$9.67 \cdot 10^{12}$	$8.68 \cdot 10^{12}$
R_3	$1.40 \cdot 10^{13}$	$3.20 \cdot 10^{13}$	$2.43 \cdot 10^{13}$	$4.19 \cdot 10^{13}$

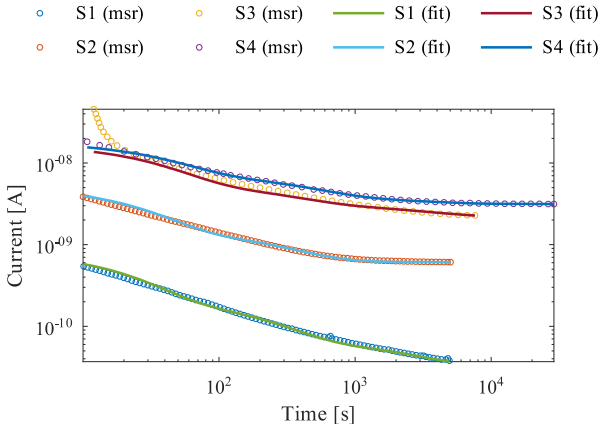

Fig. 3. Fitting of the polarization currents measured in [18, 19, 20]. The agreement between the measured (msr) and the fitted (fit) curves confirms the validity of the Occhini circuit.

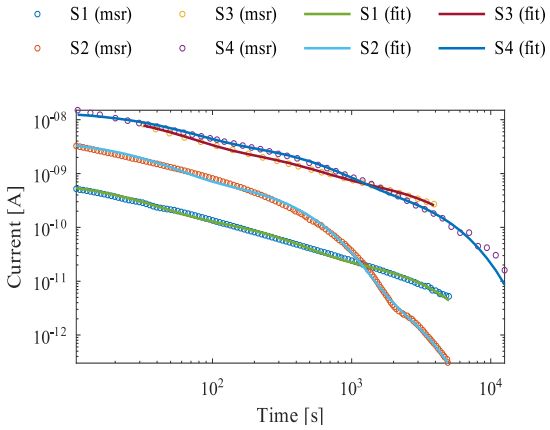

Fig. 2. Fitting of the depolarization currents measured in [18, 19, 20]. The curves of S1, S2 and S3 are reported in their respective papers. As for S4, only the polarization current was available: the depolarization one was obtained by subtracting the steady-state current from the measured one. The agreement between the measured (msr) and the fitted (fit) curves confirms the validity of the Occhini circuit.

The results presented so far have been validated for transients up to 10^4 s. In case of longer transients, lasting days or even weeks, to fit the long-term currents it may be necessary to add more R_k–C_k branches to the model. If the polarization processes at such long times are still predominant (as e.g. in the case of interface polarization), then the model is valid also in this time range. This requires, however, more extensive experimental validation.

Fig. 3 compares the fitted polarization curves ("fit") with the measured ones ("msr"). Simulations are performed using the 3 branches fitted from the depolarization curves, and the good agreement with the experiments confirms the robustness of the the Occhini circuit. The remaining parameters R_∞ and C_∞, needed to complete the model, are listed in Table 5: resistances R_∞ are obtained from the steady–state polarization currents, while only the capacitance of sample S3 was available from [18] (this is, however, not an issue, because to simulate the

currents in Fig. 2 and Fig. 3 only the response of the R_k–C_k branches is useful). The applied voltage is also added to the table in order to complete the set of data needed to reproduce the simulations.

TABLE V
PARAMETERS FITTED FROM MEASUREMENTS IN [18, 19, 20]

	S1	S2	S3	S4
R_∞ [Ω]	$1.58 \cdot 10^{13}$	$8.19 \cdot 10^{11}$	$1.10 \cdot 10^{13}$	$9.71 \cdot 10^{12}$
C_∞ [F]	–	–	$2.79 \cdot 10^{-10}$	–
V [kV]	0.5	0.5	24	30.6

In conclusion, the robustness of the Occhini circuit in the description of polarization processes under different working conditions seems to be fully supported.

III. FINITE DIFFERENCE SCHEME FOR SEMI–DISCRETIZATION IN SPACE

In this section we perform the 1D finite difference discretization of a DC cable insulation, which is modeled with (2) and (3): this allows to evaluate the impact of polarization processes on the electric field transient. In the next section we will show that the same discretization can be represented by the Occhini circuit, providing then a link between the numerical model and the fitting of parameters ε, σ, τ_k and χ_k presented in the previous section. For the purpose of this study the DC cable is modelled using the simplified structure depicted in Fig. 4, where the central conductor and the surrounding insulation are taken into consideration. Considering the cable symmetry, we can limit the investigated geometry to the cross-section. The domain is, therefore, axisymmetric, and all the vector fields in (2) and (3) have only the radial component: $\boldsymbol{E} = E\boldsymbol{u}_r = -\partial_r\varphi\boldsymbol{u}_r$ and $\boldsymbol{P}_k = P_k\boldsymbol{u}_r$. Thus, (3) can be written as

$$\begin{cases} \rho = \frac{1}{r}\frac{\partial}{\partial r}\left(-\varepsilon_\infty r\frac{\partial\varphi}{\partial r} + r\sum_{k=1}^{3}P_k\right) \\ \tau_k\frac{\partial P_k}{\partial t} + P_k + \varepsilon_0\chi_k\frac{\partial\varphi}{\partial r} = 0 \quad k = 1,\dots,3 \\ \frac{\partial\rho}{\partial t} - \frac{1}{r}\frac{\partial}{\partial r}\left(\sigma r\frac{\partial\varphi}{\partial r}\right) = 0 \end{cases} . \tag{8}$$

Before proceeding with the discretization of (8) it is convenient to transform each equation by means of a suitable scaling and change of variables. Substituting the first equation of (8) into the last, it becomes

$$\begin{cases} \tau_k\frac{\partial P_k}{\partial t} = -P_k - \varepsilon_0\chi_k\frac{\partial\varphi}{\partial r} \quad k = 1,\dots,3 \\ \frac{\partial}{\partial t}\left(\frac{1}{r}\frac{\partial}{\partial r}\left(-\varepsilon_\infty r\frac{\partial\varphi}{\partial r} + r\sum_{k=1}^{3}P_k\right)\right) - \frac{1}{r}\frac{\partial}{\partial r}\left(\sigma r\frac{\partial\varphi}{\partial r}\right) = 0 \end{cases} . \tag{9}$$

Swapping the time and space differentiation operators and regrouping yields:

$$\begin{cases} \tau_k\frac{\partial P_k}{\partial t} = -P_k - \varepsilon_0\chi_k\frac{\partial\varphi}{\partial r} \quad k = 1,\dots,3 \\ \frac{1}{r}\frac{\partial}{\partial r}\left(\frac{\partial}{\partial t}\left(-\varepsilon_\infty r\frac{\partial\varphi}{\partial r} + r\sum_{k=1}^{3}P_k\right) - \sigma r\frac{\partial\varphi}{\partial r}\right) = 0 \end{cases} . \tag{10}$$

Introducing the following auxiliary variables

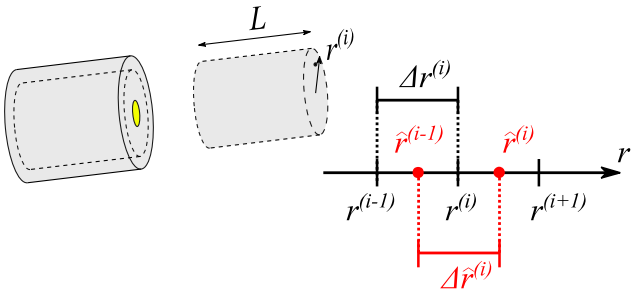

Fig. 4. Discretization of the HVDC cable insulation.

$$Q_\infty := -2\pi\,\varepsilon_\infty\,Lr\,\frac{\partial\varphi}{\partial r}\,, \tag{11}$$
$$Q_k := 2\pi\,Lr\,P_k\,, \tag{12}$$

where L is the cable length, and the following coefficients

$$\alpha := 2\pi\,\varepsilon_\infty\,Lr\,, \tag{13}$$
$$\beta_k := 2\pi\,\varepsilon_0\chi_k\,Lr\,, \tag{14}$$
$$\gamma := 2\pi\,Lr\,\sigma\,, \tag{15}$$

the following system of equations is obtained:

$$\begin{cases} Q_\infty = -\alpha\,\frac{\partial\varphi}{\partial r} \\ \tau_k\frac{\partial Q_k}{\partial t} = -Q_k - \beta_k\frac{\partial\varphi}{\partial r} \quad k = 1,\dots,3 \\ \frac{\partial}{\partial r}\left(\frac{\partial}{\partial t}\left(Q_\infty + \sum_{k=1}^{3}Q_k\right) - \gamma\,\frac{\partial\varphi}{\partial r}\right) = 0 \end{cases} . \tag{16}$$

which needs to be solved in the interval $I = \{r_{min} \le r \le r_{max}\}$ for time $t < T$.

We can now proceed with the semi–discretization of (9) in space, using suitable centered finite difference formulas as follows. We partition I into N subintervals by means of $N+1$ grid nodes, $r^{(0)} = r_{min} < r^{(1)} < \dots < r^{(i)} < \dots < r^{(N)} = r_{max}$, and define the subinterval lengths and midpoints (Fig. 4)

$$\Delta r^{(i)} := r^{(i+1)} - r^{(i)}\,, \tag{17}$$
$$\hat{r}^{(i)} = \frac{r^{(i)} + r^{(i+1)}}{2}\,, \tag{18}$$
$$\Delta\hat{r}^{(i)} := \hat{r}^{(i)} - \hat{r}^{(i-1)}\,. \tag{19}$$

We collocate the coefficients at the midpoints by letting:

$$\alpha^{(i)} := 2\pi\,\varepsilon_\infty\,L\hat{r}^{(i)}\,, \tag{20}$$
$$\beta_k^{(i)} := 2\pi\,\varepsilon_0\chi_k\,L\hat{r}^{(i)}\,, \tag{21}$$
$$\gamma^{(i)} := 2\pi\,L\hat{r}^{(i)}\,\sigma\left(\hat{r}^{(i)}\right). \tag{22}$$

Assuming $f(r)$ to be a smooth function over the interval I and denoting its nodal values over the grid as $f^{(i)} := f\left(r^{(i)}\right)$ and $\hat{f}^{(i)} := f\left(\hat{r}^{(i)}\right)$ we let

$$\left(\frac{\partial f}{\partial r}\right)\left(r^{(i)}\right) \simeq \frac{f^{(i+1)} - f^{(i)}}{\Delta r^{(i)}}\,, \tag{23}$$
$$\left(\frac{\partial f}{\partial r}\right)\left(\hat{r}^{(i)}\right) \simeq \frac{\hat{f}^{(i+1)} - \hat{f}^{(i)}}{\Delta\hat{r}^{(i)}}\,, \tag{24}$$

and, applying such formulas to (16), we obtain

$$\begin{cases} Q_\infty^{(i)} = -\frac{\alpha^{(i)}}{\Delta r^{(i)}}\left(\varphi^{(i+1)} - \varphi^{(i)}\right) \\ \tau_k \dot{Q}_k^{(i)} = -Q_k^{(i)} - \frac{\beta_k^{(i)}}{\Delta r^{(i)}}\left(\varphi^{(i+1)} - \varphi^{(i)}\right) \quad k = 1, \dots, 3 \\ \frac{1}{\Delta \hat{r}^{(i)}}\Big(\left(\dot{Q}_\infty^{(i)} + \sum_{k=1}^{3} \dot{Q}_k^{(i)}\right) - \left(\dot{Q}_\infty^{(i-1)} + \sum_{k=1}^{3} \dot{Q}_k^{(i-1)}\right) - \\ \left(\frac{\gamma^{(i)}}{\Delta r^{(i)}}\left(\varphi^{(i+1)} - \varphi^{(i)}\right) - \frac{\gamma^{(i-1)}}{\Delta r^{(i-1)}}\left(\varphi^{(i)} - \varphi^{(i-1)}\right)\right)\Big) = 0. \end{cases} \tag{25}$$

Introducing the quantities

$$C_\infty^{(i)} := \frac{\alpha^{(i)}}{\Delta r^{(i)}}, C_k^{(i)} := \frac{\beta_k^{(i)}}{\Delta r^{(i)}}, \tag{26}$$

$$G^{(i)} := \frac{\gamma^{(i)}}{\Delta r^{(i)}}, \tag{27}$$

that are dimensionally capacitance and conductance, respectively, we end up with

$$\begin{cases} Q_\infty^{(i)} = -C_\infty^{(i)}\left(\varphi^{(i+1)} - \varphi^{(i)}\right) \\ \tau_k \dot{Q}_k^{(i)} = -Q_k^{(i)} - C_k^{(i)}\left(\varphi^{(i+1)} - \varphi^{(i)}\right) \quad k = 1, \dots, 3 \\ \left(\dot{Q}_\infty^{(i)} + \sum_{k=1}^{3} \dot{Q}_k^{(i)}\right) - \left(\dot{Q}_\infty^{(i-1)} + \sum_{k=1}^{3} \dot{Q}_k^{(i-1)}\right) - \\ \left(G^{(i)}\left(\varphi^{(i+1)} - \varphi^{(i)}\right) - G^{(i-1)}\left(\varphi^{(i)} - \varphi^{(i-1)}\right)\right) = 0. \end{cases} \tag{28}$$

Equation (10) constitutes a system of differential-algebraic equations (DAE) that can be solved via suitable time-stepping methods, the most commonly used being backward difference formulas (BDF) [20].

IV. Relation between the Semi–Discretized Model and the Occhini Circuit

In this section we show the equivalence of the semi–discretized system of equations (10), and the Occhini circuit, with suitable identification of the model parameters. The importance of such an identification is twofold: on one hand it allows to determine the physical parameters of (3) from charging and discharging current measurements of thin samples as in [8, 9], while, on the other hand, it allows to perform simulations of non–flat and non–uniform geometries, such as the insulation layer of a DC cable with non–uniform temperature distribution.

Consider the circuit of Fig. 5, and let us write the Kirchhoff current law at the i–th node

$$\left(\dot{Q}_\infty^{(i)} + \sum_{k=1}^{3} \dot{Q}_k^{(i)}\right) - \left(\dot{Q}_\infty^{(i-1)} + \sum_{k=1}^{3} \dot{Q}_k^{(i-1)}\right) - \left(G^{(i)}\left(\varphi^{(i+1)} - \varphi^{(i)}\right) - G^{(i-1)}\left(\varphi^{(i)} - \varphi^{(i-1)}\right)\right) = 0\,. \tag{29}$$

Defining the capacitance charges as

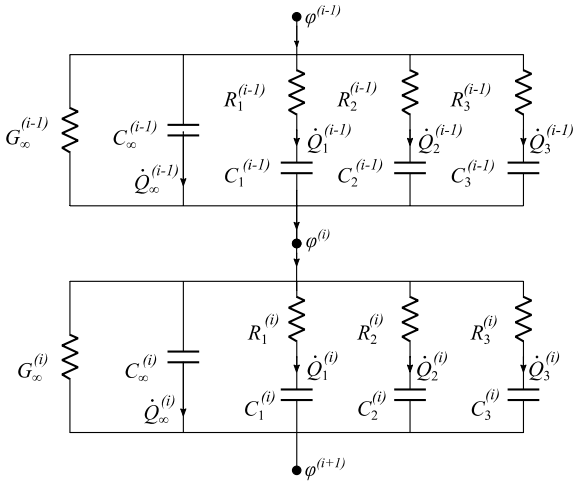

Fig. 5. Series of Occhini circuits. This configuration is equivalent to the finite difference scheme derived in section III.

$$Q_\infty^{(i)} = -C_\infty^{(i)}\left(\varphi^{(i+1)} - \varphi^{(i)}\right), \tag{30}$$

$$Q_k^{(i)} = -C_k^{(i)}\left(\varphi^{(i+1)} - \varphi_k^{(i)}\right), \tag{31}$$

and solving for the nodal voltages $\varphi_k^{(i)}$ in terms of the branch currents $\dot{Q}_k^{(i)}$ we obtain

$$\frac{C_k^{(i)}}{G_k^{(i)}} \dot{Q}_k^{(i)} = -Q_k^{(i)} - C_k^{(i)}\left(\varphi^{(i+1)} - \varphi^{(i)}\right), \tag{32}$$

Equations (30) and (29) are equivalent to the first and the third equations in (28), respectively. Equation (32) is equivalent to the second equation in (28) if we let

$$G_k^{(i)} := \frac{C_k^{(i)}}{\tau_k}. \tag{33}$$

In conclusion, Table 6 compares the expressions for the conductivities and the capacitances derived in this section, which refer to the axisymmetric geometry of the cable, and the ones of the flat sample provided in section 2, which refer to a planar geometry. One can note that the physical parameters ε, σ, χ_k and τ_k are the same, while the geometric factors change.

TABLE VI
RELATION OF CIRCUIT ELEMENTS TO MATERIAL PHYSICAL PARAMETERS OF A FLAT SAMPLE WITH AREA A AND THICKNESS d, AND A THIN LAYER OF AXISYMMETRIC CABLE INSULATION OF THICKNESS Δr AT DISTANCE r FROM THE CABLE AXIS.

Parameter	Cable	Flat sample
G_∞	$2\pi L \frac{Lr}{\Delta r}\sigma(r)$	$\sigma \frac{A}{d}$
C_∞	$2\pi \frac{Lr}{\Delta r}\varepsilon_\infty$	$\varepsilon_\infty \frac{A}{d}$
C_k	$2\pi \frac{Lr}{\Delta r}\varepsilon_0 \chi_k$	$\varepsilon_0 \chi_k \frac{A}{d}$
G_k	$\frac{C_k}{\tau_k}$	$\frac{C_k}{\tau_k}$

V. Numerical Results

In this section we simulate the electric field transient in a HVDC cable with a nominal voltage of V_n = 300 kV, a conductor radius of 23 mm and an insulation thickness of d = 20 mm. We consider two different cables in which the insulation is constituted by the multi–layer materials of S3 and S4 discussed in section 2 (which represent better a real DC cable insulation system). The electrical conductivity for both materials is assumed to be only temperature–dependent:

$$\sigma(T) = \sigma_0 \exp\left[-\alpha\left(\frac{1}{T} - \frac{1}{T_{ref}}\right)\right]. \tag{34}$$

The same α is adopted for both materials, using a typical value for impregnated paper [8], while $\sigma_0 = \sigma(T_{ref})$ is computed from (7), using the resistance values of Table 5. The parameters to model the conductivity of S3 and S4 are resumed in Table 7. The value of T_{ref} is taken from Table I. Note that both T and T_{ref} in (34) must be in kelvin.

TABLE VII
Conductivity model parameters for materials S3 and S4

Material	α [K]	σ_0 [S/m]	T_{ref} [°C]
S3	$1.01 \cdot 10^4$	$1.01 \cdot 10^{-14}$	20
S4	$1.01 \cdot 10^4$	$3.28 \cdot 10^{-14}$	50

As for the dielectric properties of the two materials, reference is made to section 2, but some assumptions were required since not all the necessary data was available. First, permittivity ε_∞ associated to the fast polarization processes is assumed to be the same for both S3 and S4. Capacitance $C_\infty = 2.79 \cdot 10^{-10}$ F of S3 is given in Table 5, and, through (6), it corresponds to $\varepsilon_\infty = 3.5\varepsilon_0$. Such a value is typical of impregnated paper, and it is used also for S4. Susceptibilities χ_k were retrieved from the C_k via (8). Table 8 lists the χ_k obtained for the two materials.

TABLE VIII
Susceptibilities for materials S3 and S4

Material	χ_1	χ_2	χ_3
S3	0.21	0.39	1.6
S4	0.51	1.7	2.4

Lacking measurements of polarization and depolarization currents at different temperatures, we assume that, except for the conductivity, all other properties of S3 and S4 are temperature independent. In the following discussion we distinguish between C1, which is a cable that uses S3 as insulating material, and C2, which is the same cable but with S4 as insulating material. Both cables are simulated assuming the same temperature distribution across the insulation, with T_{int} = 55°C and T_{ext} = 25°C. This also fixes the distribution of the electric conductivity.

The simulated transient is made of three consecutive stages: energization (from 0 to V_n), polarity inversion (from V_n to $-V_n$) and discharge (from $-V_n$ to 0). The commutations occur, respectively, at 0 hours, 36 hours and 72 hours. The voltage step at each commutation is modeled with a ramp, from 0 to V_n within 2 s and from V_n to $-V_n$ withing 2 s [21]. For each cable two simulations were performed: one using the standard model (1), and the other with the polarization model (3). To show the differences between the models' predictions (during the transients), the field difference was defined as:

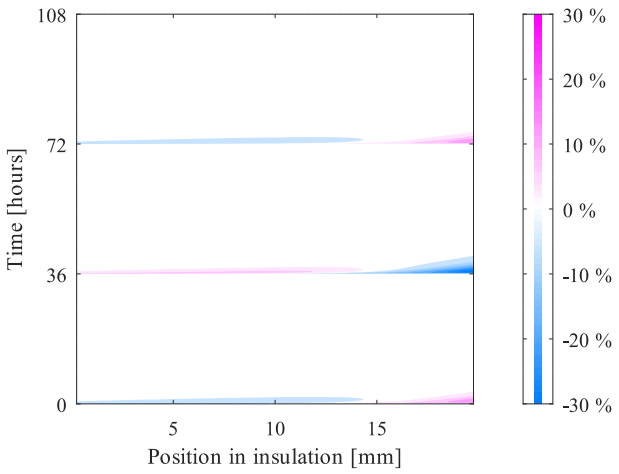

Fig. 6. Field difference $\Delta E(r,t)$ for cable C1, from transient to steady state. The differences between E_{pol} and E_{std} persist for a few hours and the highest ones are reached after the polarity inversion.

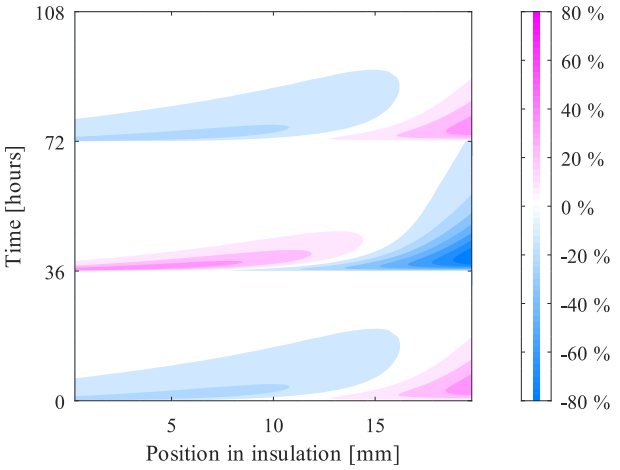

Fig. 7. Field difference $\Delta E(r,t)$ for cable C2, from transient to steady state. The differences between E_{pol} and E_{std} persist for much more time than in C1, and they are greater.

$$\Delta E(r,t) = \frac{E_{pol}(r,t) - E_{std}(r,t)}{E_{avg}}, \tag{35}$$

where $E_{pol}(r,t)$ and $E_{std}(r,t)$ are computed from (3) and (1), respectively, and $E_{avg} = V_n / d = 15$ kV/mm is the average insulation electric field.

Figs. 6 and 7 report $\Delta E(r,t)$ for C1 and C2, respectively. In both cases the largest differences occur immediately after each commutation, because $E_{std}(r,t)$ evolves faster that $E_{pol}(r,t)$, which is, in turn, slowed by the polarization dynamic. The white

regions in Figs. 6 and 7 correspond to the condition $\Delta E(r,t) = 0$: this means that the field distribution in each cable, computed by the two models, has the same profile and the same time evolution. It is noticeable that $\Delta E(r,t)$ displays considerably large values: in C1 the maximum value is 5 kV/mm, while in C2 it is 12 kV/mm. These values are reached, respectively, 0.7 hours and 4 hours after the polarity inversion, which occurs 36 hours after the energization.

Fig. 8 shows the electric field profiles at the end of the energization transient, before the polarity inversion. The fields were computed using the polarization model (p), and the standard one (s), for both cables. As we mentioned, such profiles correspond to the steady-state resistive distribution, which is governed by the same equation in both models:

$$\nabla \cdot (\sigma \boldsymbol{E}) = 0 \;\Leftrightarrow\; \nabla \cdot \left(e^{-\alpha/T}\boldsymbol{E}\right) = 0\,. \tag{36}$$

Since we assumed the same α for both insulation materials, and since both cables have the same temperature distribution, the resistive profiles in Fig. 8 are all the same.

Fig. 9 shows the field profiles of the two cables, computed again by the polarization (p) and standard (s) models, 2 hours after the polarity inversion. The fact that, at a given time instant, the field profiles differ from each other, is another indication that the transient duration is different in each cable. Of course, the duration changes also according to the model used for the simulation, as highlighted by Figs. 6 and 7. Therefore, Fig. 9 can be used to understand how fast the electric field evolves for the insulating material and the model employed for the simulation. Ideally, a precise comparison should be based on the calculation of a time constant τ that is representative of the transient duration. Such a quantity can be, in fact, calculated for the standard model (1), where τ is obtained as the ratio between permittivity and conductivity: in this way we can compare the time constants of C1 (s) and C2 (s). Considering, indeed, that both C1 (s) and C2 (s) are computed using the standard model, with the same α and the same temperature profile, but with different T_{ref}, we have:

$$\frac{\tau_{C2\,(s)}}{\tau_{C1\,(s)}} = \frac{\varepsilon/\sigma_{S4}}{\varepsilon/\sigma_{S3}} = \frac{\sigma_{S3}e^{\alpha/T_{ref,S3}}}{\sigma_{S4}e^{\alpha/T_{ref,S4}}} \simeq 7, \tag{37}$$

meaning that the electric field transient in C2 (s) is slower than in C1 (s). This is coherent with Fig. 9, where the profile of C1 (s) is already inverted with respect to the starting configuration of Fig. 8, while the field in C2 (s) is still inverting. As for the fields in C1 (p) and C2 (p), the analysis is more difficult because the polarization model (3) involves more than one time constant: we have the τ calculated as ε/σ, but also the time constants of the polarization processes. It is therefore impossible to derive a single time constant that represents the field transient. On the other hand, we can make some qualitative considerations. Comparing C2 (s) and C2 (p) in Fig. 9, we observe that C2 (p) lags C1 (s). In the same way, C1 (p) lags C1 (s). This indicates that the field evolution computed with the polarization model (p) is slower than the one computed with the standard model (s). The polarization processes slow down the electric field evolution in the cable.

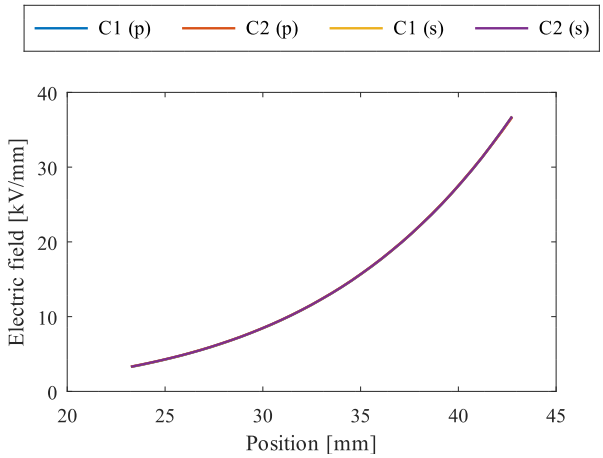

Fig. 8. Resistive field profiles at the end of the energization transient, and just before the polarity inversion, computed using the polarization (p) and the standard model (s).
All the curves are overlapped because, at steady state, all models satisfy equation (33).

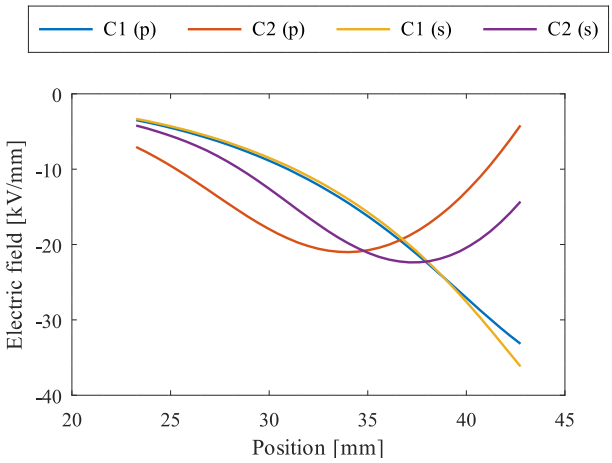

Fig. 9. Field profiles 2 hours after the polarity inversion, computed using the polarization (p) the standard model (s).

Fig. 10 shows the maximum electric field in the insulation of C1 and C2 during the transient,

$$E_m(t) = \max_r |E(r,t)|\,, \tag{38}$$

with $E(r,t)$ being the field computed using either the polarization (E_{pol}) or the standard (E_{std}) model. During the energization and polarity inversion transients, before reaching the steady state, $E_m(t)$ computed using the polarization model (p) is lower than the one computed with the standard model (s), and this happens for both C1 and C2. During the discharge transient the opposite situation occurs. This finding highlights the very contribution of polarization processes to the field transient in a HVDC cable: under the application of a DC voltage, the maximum field intensity experienced by the cable during the transient is lower in the presence of polarization

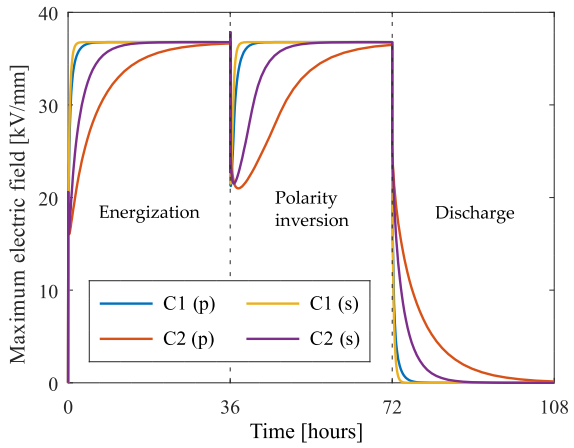

Fig. 10. Maximum electric fields in C1 and C2 during the simulated transient, computed using the polarization model (p) and the standard one (s).

processes. At steady state the maximum field is the same for both models, as already derived from equation (33). In conclusion, the cable works under reduced stress with respect to the steady–state condition for longer time in the presence of polarization processes.

VI. Conclusion

This paper presents a new approach to the simulation of electric field transients in DC cables, including the dynamic of dielectric polarization processes in the standard model (1).

To perform consistent and robust simulations, we must, first, infer the polarization parameters χ_k and τ_k from the experimental measurements of polarization and depolarization currents of flat samples of dielectric materials. The Occhini circuit works well to identify the parameters of the most significant polarization processes that govern the PDC dynamic.

The second step is to use the inferred parameters to simulate the electric field transients in the cable. This can be done if the Occhini circuit is linked to the differential model (3). To this aim, this paper demonstrates that the Occhini circuit is indeed equivalent to the finite difference discretization of (3).

The final step is the field simulation. This paper shows that the differences between the predictions of the standard model and those of the polarization model can be remarkable, depending on the field transient duration. During transients, the maximum electric field experienced by the cable under the application of a DC voltage is lower in the presence of polarization processes. This can impact on design and evaluation of intrinsic and extrinsic aging, especially when partial discharges phenomena can be involved in transient, rather than in steady-state conditions.

References

[1] G. C. Montanari, P. Morshuis, P. Seri, and R. Ghosh, “Ageing and reliability of electrical insulation: the risk of hybrid AC/DC grids,” *High Voltage*, vol. 5, no. 5, pp. 620–627, Oct. 2020.

[2] M. J. P. Jeroense and P. H. F. Morshuis, “Electric fields in HVDC paper-insulated cables,” *IEEE Trans. Dielectr. Electr. Insul.*, vol. 5, no. 2, pp. 225–236, Apr. 1998.

[3] H. F. Morshuis and J. J. Smit, “Partial discharges at DC voltage: their mechanism, detection and analysis,” *IEEE Trans. Dielectr. Electr. Insul.*, vol. 12, no. 2, pp. 328–340, Apr. 2005.

[4] G.C. Montanari, R. Ghosh, H. Naderiallaf and P. Seri, 2021, "Reliability of HVDC and MVDC electrical asset: the challenge of insulation design", *ICPADM*, pp. 1-8, Malaysia, July 2021.

[5] G.C. Montanari, R. Hebner, P. Seri and R. Ghosh, 2020, "Self-assessment of health conditions of electrical assets and grid components: a contribution to smart grids", *IEEE Trans. on Smart Grid*, pp. 1-8, 2021.

[6] H. Naderiallaf, P. Seri and G.C. Montanari, "DC cables and partial discharge phenomenology during voltage transients: effect of voltage slew rate.", *IEEE Trans. on Power Delivery*, pp. 1-8, 2021.

[7] C. K. Eoll, “Theory of stress distribution in insulation of high voltage d.c. cables. Part I,” *IEEE Trans. Electr. Insul.*, El-10 (2) (1975) 27–35.

[8] E. Occhini and G. Maschio, “Electrical characteristics of oil impregnated paper as insulation for HV DC cables,” in *IEEE Transactions on Power Apparatus and Systems*, vol. PAS-86, no. 3, pp. 312-326, 1967.

[9] P. Cambareri, C. de Falco, L. Di Rienzo, P. Seri and G. C. Montanari, “Charging and discharging current measurements and impact of polarization dynamics on electric field modeling in HVDC paper–insulated cables,” in *IEEE Access*, vol. 9, pp. 45155–45162, 2021.

[10] A. K. Jonscher, *Dielectric relaxation in solids*, Chelsea Dielectric Press Ltd, London, 1983.

[11] S. J. Frobin, C. Freye, C. F. Niedik and F. Jenau, “Generic field simulation framework for HVDC cables,” in *IEEE 2nd International Conference on Dielectrics*, Budapest, Hungary, 2018.

[12] C. Jorgens, F. Kasolis and M. Clemens, “Numerical simulations of temperature stability limits in high-voltage direct current cable insulations,” *IEEE Trans. Magn.*, vol. 55, no. 6, 1–4, 2019.

[13] V. D. Houhanessian, “Measurement and analysis of dielectric response in oil–paper insulation systems,” 1998.

[14] I. Wirth, M. H. Zink, A. Kuechler, F. Berger and T. Schnitzler, “Implementation of conduction and polarization mechanisms in transient FEM simulations of HVDC insulation systems,” *VDE High Voltage Technology 2018*; *ETG-Symposium*, Berlin, Germany, 2018, pp. 1–6.

[15] T. Zhou, P. Bidan, L. Laudebat and M.-L. Locatelli, “Time domain simulation of insulating dielectric materials with non-instantaneous polarization,” *COMSOL Conference 2020 Europe*, Grenoble (virtual), France, 2020.

[16] P. Cambareri, C. de Falco, L. Di Rienzo, P. Seri and G. C. Montanari, “Simulation and modelling of transient electric fields in HVDC insulation systems based on polarization current measurements,” in *Energies*, vol. 14, no. 24, 8323, 2021.

[17] P. Cambareri, C. de Falco, L. Di Rienzo, P. Seri and G. C. Montanari, “Reduced-parameter modelling of polarization and depolarization currents in polymeric materials under low electric fields,” submitted.

[18] J. Wei, G. Zhang, H. Xu, H. Peng, S. Wang and M. Dong, “Novel characteristic parameters for oil-paper insulation assessment from differential time-domain spectroscopy based on polarization and depolarization current measurement,” in *IEEE Trans. Dielectr. Electr. Insul.*, vol. 18, no. 6, pp. 1918–1928, 2011.

[19] R. Wiengarten, F. Jenau and B. Bakija, “Polarization and depolarization behavior of various oil impregnated paper insulations stressed by very high DC field strength,” *Proc. 17th Int. Symp. High Voltage Eng.*, 2011.

[20] G. Hakonseth and E. Ilstad, “Time–dependent electric field distribution in layered paper–oil insulation,” *Proceedings of the 26th Nordic Insulation Symposium*, No. 26, 2019.

[21] J. LeVeque, *Finite difference methods for ordinary and partial differential equations: steady-state and time-dependent problems*, Society for Industrial and Applied Mathematics, Philadelphia, PA, USA.

[22] Y. Shi, M. Zhu, Y. Chen and X. Cai, “Power flow reversal control of hybrid HVDC transmission system with LCC and FBMMC," *2020 IEEE Region 10 Cconference (TENCON)*, 2020, pp. 1295–1300.